

## Article

# Effects of Aging Treatments on the Age Hardening Behavior and Microstructures in an Al-Mg-Si-Cu Alloy

Limei Liu <sup>1</sup>, Yingpeng Hou <sup>2</sup>, Tuo Ye <sup>2</sup>, Like Zhang <sup>2</sup>, Xuan Huang <sup>2</sup>, Yuqing Gong <sup>2</sup>, Chao Liu <sup>2</sup>, Yuanzhi Wu <sup>1,2,\*</sup> and Shiyun Duan <sup>1,\*</sup>

<sup>1</sup> Research Institute of Automobile Parts Technology, Hunan Institute of Technology, Hengyang 421002, China; 2021001034@hnit.edu.cn

<sup>2</sup> College of Intelligent Manufacturing and Mechanical Engineering, Hunan Institute of Technology, Hengyang 421002, China

\* Correspondence: 2013001767@hnit.edu.cn (Y.W.); 2021001039@hnit.edu.cn (S.D.)

**Abstract:** In this study, we investigated the effects of modified aging treatments on the microstructures and hardness in a commercial 6016 Al alloy through hardness tests and transmission electron microscopy (TEM) observations. The results demonstrate that many fine needle-like  $\beta''$  phases contribute to the high hardness of peak-aged (T6) alloys. Over-aging treatments lead to the precipitation of lath-like  $\beta'$ ,  $\beta''$ /disordered, or  $B'$ /disordered composite phases. Moderate over-aging treatment results in the coarsening of grain boundary precipitates (GBPs) and widening of the precipitate-free zone (PFZ), while heavy over-aging treatment triggers the re-precipitation of Cu-containing GBPs and increases the number density of GBPs. A retrogression and re-aging (RRA) treatment precipitates  $\beta''$ , lath-like  $\beta'$ , and disordered phases, while a two-step aging (T78) treatment precipitates  $\beta''$ ,  $B'$ , and disordered phases. Both the T78 and the RRA treatments lead to the coarsening of GBPs and the widening of PFZs. The decreased hardness during over-aging treatments is attributed to a combination of coarsening intragranular precipitates and/or wider PFZs. The T78 and RRA tempers achieve 95.5% and 94% of the hardness values of the T6 treatment, respectively. The hardness values of the RRA and T78 treated alloys are related to the finer nano-sized precipitates formed during the high temperature process. These precipitates can compensate for the loss of hardness caused by the increase in the widths of the PFZs and the coarsening of the matrix precipitates. The relationship between the hardness and microstructures such as PFZs and precipitates in the matrix during various heat treatments is elucidated.

**Keywords:** 6016 alloy; T78; retrogression and re-aging; precipitation; TEM



**Citation:** Liu, L.; Hou, Y.; Ye, T.; Zhang, L.; Huang, X.; Gong, Y.; Liu, C.; Wu, Y.; Duan, S. Effects of Aging Treatments on the Age Hardening Behavior and Microstructures in an Al-Mg-Si-Cu Alloy. *Metals* **2024**, *14*, 238. <https://doi.org/10.3390/met14020238>

Academic Editor: Amogelang Bolokang

Received: 28 December 2023

Revised: 9 February 2024

Accepted: 12 February 2024

Published: 15 February 2024



**Copyright:** © 2024 by the authors. Licensee MDPI, Basel, Switzerland. This article is an open access article distributed under the terms and conditions of the Creative Commons Attribution (CC BY) license (<https://creativecommons.org/licenses/by/4.0/>).

## 1. Introduction

Al-Mg-Si-Cu alloys have extensive applications in transportation owing to their low density, high strength, good ductility, excellent weldability, and corrosion resistance [1–7]. The properties of these alloys are significantly influenced by solute segregation states. Upon undergoing artificial aging for a short period of time, Al-Mg-Si-(Cu) alloys exhibit a substantial increase in hardness. This hardening phenomenon stems from the formation and dispersion of a large number of nano-sized metastable precipitates within the aluminum matrix during the aging treatment [8–13]. These precipitates possess diverse atomic structures, resulting in variations in mechanical characteristics. Additionally, differences in atomic matching at the matrix–phase interface led to varying levels of interfacial strain. Both the nano-sized precipitates and the interfacial strain impede the movement of dislocations, thus contributing to the hardening of the materials. The widely accepted precipitation sequence in Al-Mg-Si alloys proceeds as follows: supersaturated solid solution (SSSS) → clusters → GP zones →  $\beta''$  →  $\beta'$  ( $B'/U1/U2$ ) →  $\beta$  [9,10,14–25].

In the Al-Mg-Si-Cu alloy, the inclusion of low concentrations of Cu (~0.10 wt.%) did not disrupt the precipitation sequence but did impact the kinetics and number density

of the precipitates [26]. Besides the typical fully coherent  $\beta''$  precipitates observed at the peak hardness conditions of the Al-Mg-Si alloys, a notable portion of precipitates comprising both fully coherent  $\beta''$  and disordered regions within the same precipitate needle ( $\beta''$ /disordered precipitates) was identified in the Cu-containing alloy [21]. Utilizing an uncorrected probe high-angle annular dark-field scanning transmission electron microscopy (HAADF-STEM), no Cu was discerned within the fully coherent  $\beta''$  regions, while Cu atomic columns were evident within the disordered regions. Moreover, it was observed that the disordered regions are based on the Si-network, as previously described [26]. Although the exact atomic arrangement in the latter scenario could not be ascertained, it is conjectured that the former local symmetry resembles the one previously proposed by Torsæter et al. [27]. This symmetry is absent in the bulk  $\beta''$  precipitate, potentially due to its Cu-free composition [26].

In recent years, considerable focus has been devoted to improving the heat resistance of aluminum alloys. Jonas K. Sunde discovered that two Si-rich alloys (Al-0.64Mg-0.88Si-0.09 and Al-0.72Mg-0.88Si-0.03Cu) formed hybrid  $\beta'$  and  $Q'$  phase precipitates in Al-Mg-Si(-Cu) alloys with low Cu additions during over-aging treatments [28]. Consequently, the microstructures of over-aged alloys exhibit greater complexity compared to earlier artificially aged states. Moreover, while the evolution of precipitates in the matrix has been meticulously elucidated, the microstructures of the grain boundary precipitates (GBPs) and precipitate-free zone (PFZ) during over-aging treatment in Al-Mg-Si-Cu alloys with low Cu content remain obscure.

T6-treated alloys typically exhibit high strength but are susceptible to corrosion, a characteristic closely linked to the presence of a GBP and PFZ [29]. Non-equilibrium grain boundary segregation phenomena significantly influence phase nucleation and growth, thereby critically impacting material properties such as strength, fracture toughness, fatigue resistance, and corrosion behavior. While detailed segregation studies have been conducted on cold-rolled Al alloys [4,30–33], a deeper and more comprehensive understanding of grain boundary segregation in conventionally aged Al alloys is necessary, particularly in Al-Mg-Si alloys containing Cu. In these alloys, grain boundary segregation plays a pivotal role for several reasons. Firstly, Cu enhances strength and mitigates inherent negative effects but concurrently increases the local susceptibility to corrosion in Al-Mg-Si(-Cu) alloys. Secondly, the occurrence of brittle intergranular fractures is associated with the formation of coarse incoherent GBPs and a soft PFZ under the specific conditions of heat treatment.

To address the strength–corrosion resistance trade-off in Al alloys, slight over-aging treatments such as two-step aging [30] and T78 [34,35] were developed. Multi-step aging strategies, which incorporate a retrogression and re-aging (RRA) treatment and T78 (high temperature aging followed by relatively low temperature aging), aimed to refine or eliminate grain boundary precipitates (GBPs), while preventing the coarsening of matrix precipitates. The T78 treatment has been successfully implemented in an Al-0.75Mg-0.75Si-0.8Cu [34] alloy and 6056 alloys [36]. The RRA treatment has been used in 7XXX alloys [37–41]. However, its effects on the microstructures and mechanical properties in low Cu-content Al-Mg-Si alloys remain unclear.

Due to its great comprehensive characteristics, the 6016 Al alloy is widely used in lightweight vehicles. Presently, research efforts primarily concentrate on the paint bake strengthening performance of this alloy, with insufficient attention given to the effects of T78 and RRA heat treatment processes on its performance and microstructures. In this study, we investigate the microstructures of intragranular precipitates, GBPs, and the PFZ adjacent to the grain boundaries in a 6016 Al alloy subjected to various heat treatments. Furthermore, we examine the relationship between hardness and microstructures in detail.

## 2. Materials and Methods

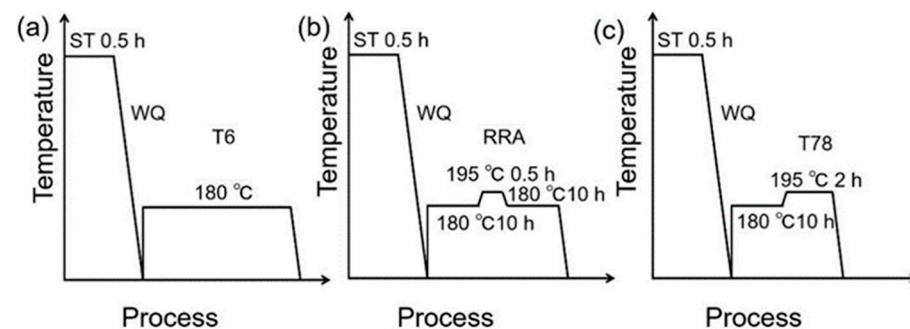
In this study, rolled commercial 6016 sheets with a thickness of 1 mm were utilized. The detailed composition of the alloy is provided in Table 1.

**Table 1.** Alloy compositions of a commercial 6016 sheet.

Alloy	Mg	Si	Cu	Al
6016	0.4	1.0	0.2	balance

These sheets underwent a solution heat treatment at 565 °C for 30 min, followed by water quenching to room temperature, and immediate aging in an oil bath at 180 °C for varying durations. The T78 treatment involved solution treatment and water quenching, followed by aging at 180 °C for 10 h, and subsequent aging at 195 °C for 2 h. It is worth noting that for retrogression temperatures exceeding 200 °C, RRA treatment cannot be applied to large-section Al alloys due to the constraint of insufficient retrogression time to simultaneously heat the surfaces and interiors of the materials.

The Al-Mg-Si alloy, typically used in automobile body structures as thin plates subjected to rolling and stamping processes with extensive surface areas, requires painting before usage. Paint baking temperatures and durations typically range around 180 °C and 30 min, respectively [7,42]. Furthermore, it has been established that the most suitable high temperature for T78 treatment is approximately 195 °C [34]. Thus, the two-step high temperature regimen and aging duration in the RRA treatment were set at 195 °C and 30 min, respectively. Consequently, the RRA process involved solution treatment and water quenching, followed by aging at 180 °C for 10 h, subsequent re-aging at 195 °C for 30 min, and, finally, aging at 180 °C for 10 h. The specific heat treatment process is illustrated in Figure 1. The abbreviations of the heat treatments used in this paper are shown in Table 2.

**Figure 1.** Specific thermomechanical process of T6, RRA, and T78 treatments in a commercial 6016 Al alloy. (a) T6; (b) RRA; and (c) T78.**Table 2.** Abbreviations of heat treatments used in this paper.

Full Name of Heat Treatments	Abbreviations
180 °C × 10 h (peak aging)	T6
180 °C × 0.5 h (under aging)	UA
180 °C × 24 h (slight over-aging)	SOA
180 °C × 120 h (moderate over-aging)	MOA
180 °C × 240 h (heavy over-aging)	HOA
180 °C × 10 h + 195 °C × 2 h (two steps aging)	T78
180 °C × 10 h + 195 °C × 0.5 h + 180 °C × 10 h (retrogression and re-aging)	RRA

The Vickers hardness was tested with a load of 4.9 N and a dwell time of 10 s and at least five indentations were measured in each sample to obtain a reliable average value. The transmission electron microscopy (TEM) and high-resolution TEM (HRTEM) observations were performed with a FEI Talos F200S G2 TEM (TEM, Talos F200S, FEI Ltd., Pleasanton, CA, USA) operated at 200 kV. All microstructure images were taken along a  $\langle 001 \rangle_{\text{Al}}$  zone axis. TEM thin foils were eventually prepared by twin-jet electro-polishing with a solution of 30% nitric acid in methanol below  $-25$  °C at an operating voltage of 15 V.

### 3. Results and Discussion

#### 3.1. Age Hardening Response of Various Heat Treatments

Figure 2a illustrates the evolution of hardness for samples artificially aged (AA) at 180 °C for various durations. It is evident that the hardness initially experiences rapid escalation with a prolonged AA time until reaching peak-aged status after 1 h. Subsequently, the peak hardness persists for a short period from 1 to 10 h, followed by a gradual decline in hardness as the AA time extends to 240 h.

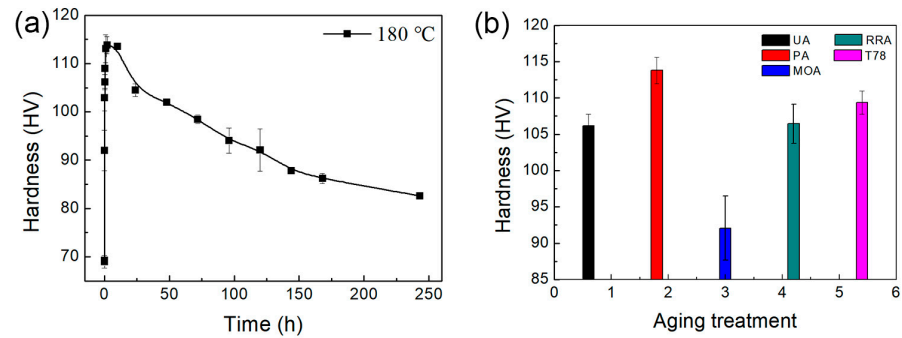


**Figure 2.** Hardness vs. artificial aging time of T6 treatment (a); and (b) hardness vs. aging treatment of UA, T6, MOA, RRA, and T78.

In Figure 2b, the hardness values of the samples subjected to RRA and T78 treatments are compared with those under UA, PA, and MOA tempers. It is observed that the hardness of the RRA and T78-treated samples is slightly lower than that of the T6-treated samples.

#### 3.2. TEM and HRTEM Overviews of Precipitates Distributed in the Matrix

Figure 3 presents typical bright-field microstructures of an AA6016 alloy subjected to T6, T78, RRA, and over-aging tempers. High-resolution transmission electron microscopy (HRTEM) characterizations were additionally conducted on the same specimens depicted in Figure 3a–c to further discern the crystal structures and types of precipitates.

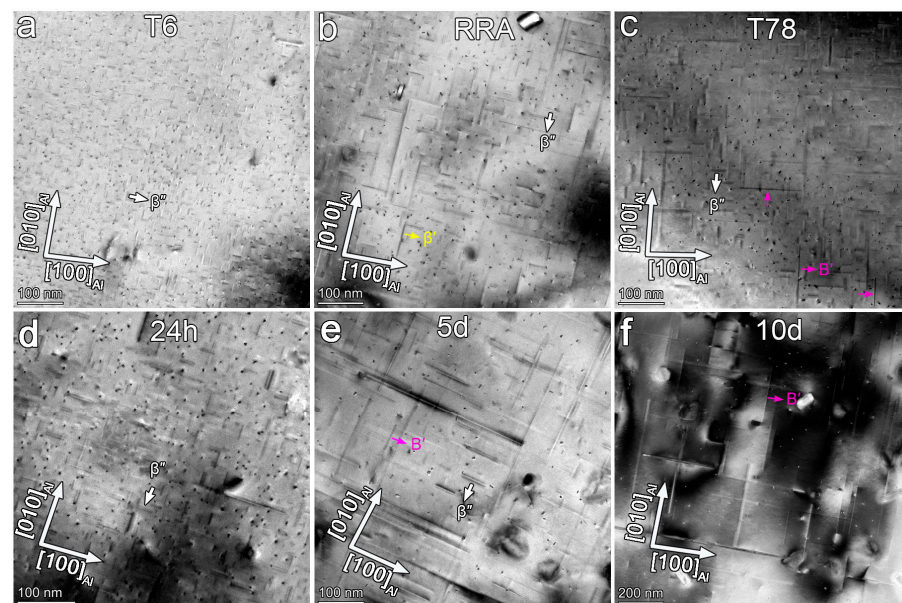


**Figure 3.** TEM bright-field images, recorded in a  $\langle 001 \rangle_{Al}$  zone axis of (a) T6; (b) RRA; (c) T78 tempers; (d) SOA; (e) MOA; and (f) HOA.

In Figure 3a, the primary precipitates observed in the T6 samples are indicated by white arrows, identified as needle-like  $\beta''$  precipitates. Furthermore, small GP zones are

still present within the matrix. The HRTEM images in Figure 4 confirm that the GP zones and  $\beta''$  phases are uniformly dispersed and coherent with the matrix. The black dots observed in Figure 3a are likely the  $\beta''$  phase viewed edge-on. These observations are consistent with previous investigations [8,10,15,21].

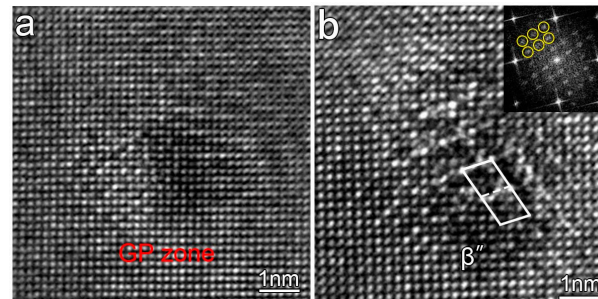


**Figure 4.** HRTEM images of the typical precipitates in T6 samples. (a) GP zone; and (b) needle-like  $\beta''$  phase. The electron beam is parallel to the  $\langle 001 \rangle_{\text{Al}}$  orientation.

To investigate the precipitation behavior of the RRA and T78 temper-treated alloys, the microstructures of samples subjected to a two-step artificial aging process—aged at 180 °C for 10 h and subsequently aged at 195 °C for 0.5 h—were examined. The main precipitates observed are the GP zones and needle-like  $\beta''$  phases, as depicted in Figure 5, resembling the microstructure of T6-treated alloys.

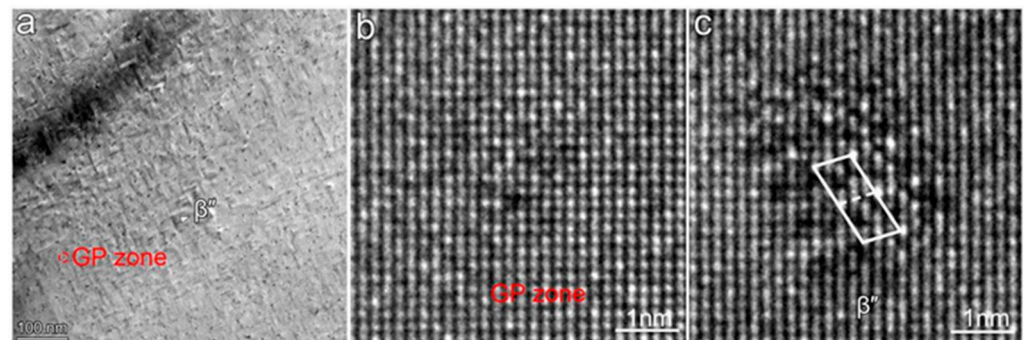


**Figure 5.** TEM images of a 6016 alloy artificial aged at 180 °C for 10 h and 195 °C for 0.5 h. (a) bright-field images; (b) GP zone; and (c) needle-like  $\beta''$  phase. The electron beam is parallel to the  $\langle 001 \rangle_{\text{Al}}$  orientation.

Following re-aging at 180 °C for 10 h, unit cells of  $\beta''$  phases are still present within the matrix (Figures 3b and 6a). Additionally, apart from the needle-like  $\beta''$  phase, lath-like phases with habit planes parallel to  $(100)_{\text{Al}}$  are also observed (Figure 6b). Although the habit plane differs from the commonly observed needle-like  $\beta'$  phase with a  $\langle 310 \rangle_{\text{Al}}$  habit plane, the lath-like phase is considered a  $\beta'$  phase. A similar lath-like  $\beta'$  phase was also observed in an over-aging treated Al-Mg-Si-Cu alloy reported by [24]. Furthermore, some phases appear almost disordered without recognizable characteristics, such as the precipitates shown in Figure 6c.

In summary, it can be concluded that the RRA treatment alters the precipitation behavior of AA6016 alloys.

Following the T78 treatment (artificial aging at 180 °C for 10 h and subsequent aging at 195 °C for 2 h), aside from the needle-like  $\beta''$  phases observed (Figures 3c and 7a), lath-like precipitates also emerge within the matrix, as indicated by the pink arrows in Figure 3c. The high-resolution TEM image of this microstructure is presented in Figure 7b. The precipitate in Figure 7b exhibits a periodicity of 0.99 nm along the  $\langle 510 \rangle_{\text{Al}}$ , consistent with one of the characteristics of the metastable  $B'$  phase [16,17,23]. Additionally, some disordered

phases lacking a long-range order also precipitate within the matrix, as shown in Figure 7c. Notably, no needle-like  $\beta'$  phase is observed in the T78-treated samples.

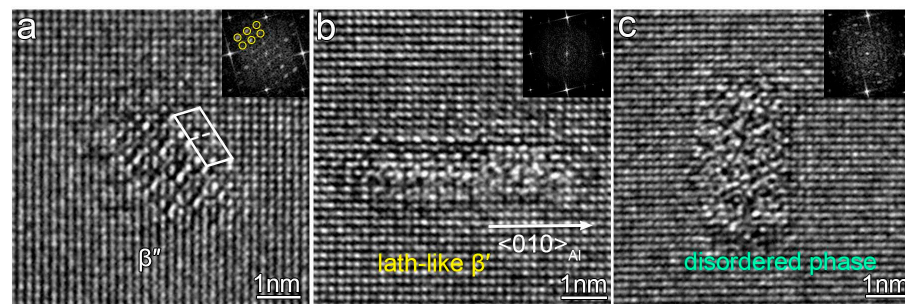


**Figure 6.** HRTEM images of the typical precipitates in a 6016-RRA alloy. The electron beam is parallel to the  $\langle 001 \rangle_{Al}$  orientation. (a) Needle-like  $\beta''$  phase; (b) lath-like  $\beta'$ ; and (c) disordered phase.

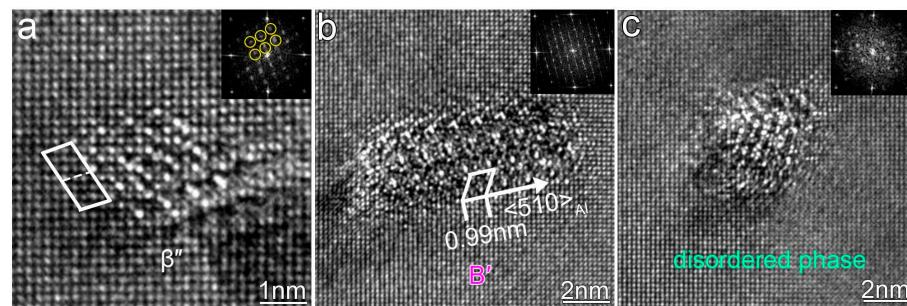


**Figure 7.** HRTEM images of the typical precipitates in a 6016-T78 alloy. The electron beam is parallel to the  $\langle 001 \rangle_{Al}$  orientation. (a) Needle-like  $\beta''$  phase; (b) lath-like  $B'$  phase; and (c) disordered phase.

Following the SOA treatment, the unit cells of precipitates other than  $\beta''$  were observed within the matrix (Figures 3d and 8a), including some  $B'$  phases (Figure 8b) and disordered phases (Figure 8c). Despite the presence of these additional precipitates, the  $\beta''$  phase remained the dominant precipitate under SOA conditions. Many precipitates exhibited moderate coarsening compared to the T6 treatment, although their sizes were nearly identical to those observed under the RRA condition.

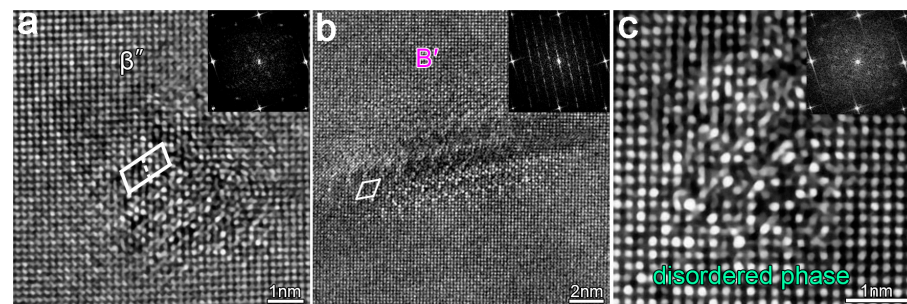


**Figure 8.** HRTEM images of the typical precipitates in a 6016-SOA alloy. The electron beam is parallel to the  $\langle 001 \rangle_{Al}$  orientation. (a) needle-like  $\beta''$  phase; (b) lath-like  $B'$  phase; (c) disordered phase.

Following the MOA treatment, a notable phase transformation of the alloys is observed, accompanied by significant coarsening of the precipitates (as depicted in Figure 3e). The high-resolution TEM (HRTEM) images (Figure 9) reveal that the main precipitates observed within the matrix are primarily needle-like  $\beta''$ /disordered composite phases, along with some lath-like  $B'$  phases exhibiting  $\{510\}_{Al}$  habit planes, and lath-like  $\beta'$  phases with  $\{100\}_{Al}$  habit planes.

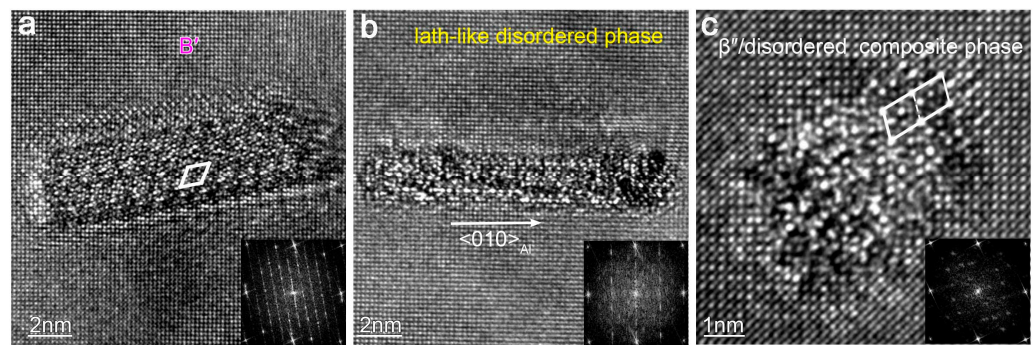


**Figure 9.** HRTEM images of the typical precipitates in a 6016-MOA alloy. The electron beam is parallel to the  $\langle 001 \rangle_{Al}$  orientation. (a) Lath-like  $B'$  phase; (b) lath-like disordered phase; and (c)  $\beta''$ /disordered composite phase.

After the HOA treatment, further coarsening of the precipitates is observed. Lath-like  $B'$  phases and  $B'$ /disordered composite phases are found in the bulk of the HOA temper. Additionally, some disordered phases lacking recognizable periodicity are observed in the bulk (as shown in Figure 10c,d).

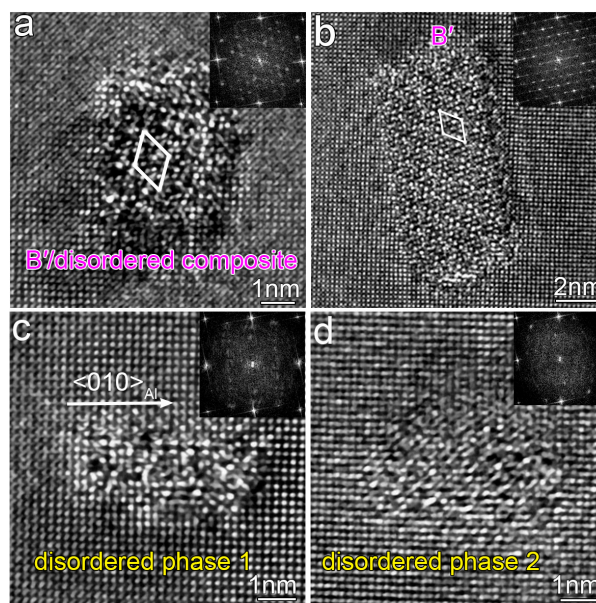


**Figure 10.** HRTEM images of the typical precipitates in a 6016 alloy over-aged at 180 °C for 10 d. The electron beam is parallel to the  $\langle 001 \rangle_{Al}$  orientation. (a) Lath-like  $B'$ /disordered composite phase; (b) lath-like  $B'$  phase; (c) disordered phase 1; and (d) disordered phase 2.

The precipitation length distributions measured on the same samples depicted in Figure 3 are illustrated in Figure 11. For each aging condition, a minimum of three TEM images were selected, with the number of precipitates considered exceeding 200 to ensure the measurement accuracy. Given that the needle-like phases are the predominant precipitate types within the matrix, the statistical analysis primarily focuses on needle-like phases rather than lath-like ones.

It is observed that the T6-treated alloy contains very fine precipitates with an average length of approximately 16 nm (Figure 8a). Compared to the T6 treated alloy, the average lengths of the  $\beta''$  phases in the 6016 alloy artificially aged at 180 °C for 10 h and 195 °C for 0.5 h increase slightly, by about 8 nm. After re-aging at 180 °C for 10 h, the average lengths of the needle-like phases increase to 48 nm.

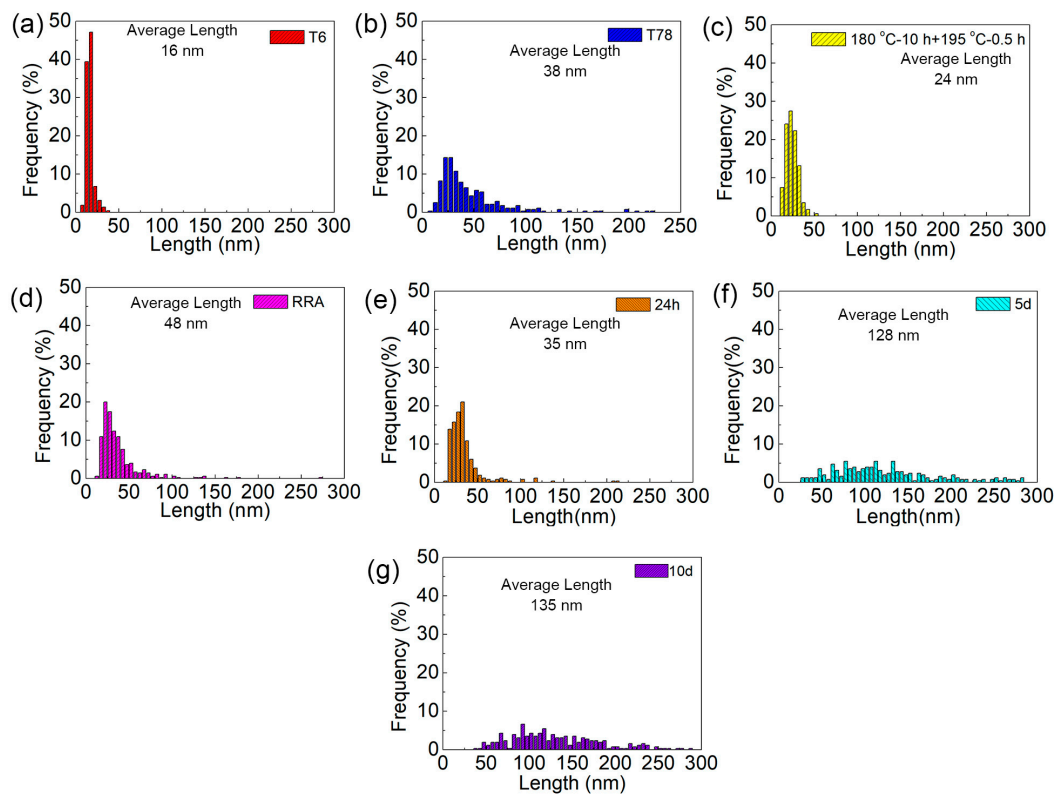


**Figure 11.** Average precipitate lengths and lengths distribution of the needle-like precipitates in the samples. (a) T6; (b) T78; (c)  $180\text{ }^{\circ}\text{C} \times 10\text{ h} + 195\text{ }^{\circ}\text{C} \times 0.5\text{ h}$ ; (d) RRA; (e) SOA; (f) MOA; and (g) HOA.

For the T78 and RRA-treated alloys, their precipitate microstructures comprise numerous relatively fine matrix precipitates and a few relatively coarse precipitates (see Table 3 and Figure 11b,d). The average length of the matrix needle-like precipitates in the T78-treated alloy is approximately 38 nm. It is noteworthy that the RRA-treated alloy exhibits more precipitates larger than 30 nm compared to the T78-treated alloy. Consequently, the matrix precipitates in the RRA-treated alloy are slightly coarser than those formed in the T78-treated alloy.

**Table 3.** Length distribution of the needle-like precipitates in the T6, RRA, T78, and over-aging treated samples.

Temper	<10 nm	10~30 nm	30~100 nm	>100 nm
T6	0.02	0.96	0.02	0.00
$180\text{ }^{\circ}\text{C} \times 10\text{ h} + 195\text{ }^{\circ}\text{C} \times 0.5\text{ h}$	0.02	0.80	0.18	0.00
RRA	0.11	0.47	0.35	0.07
T78	0.12	0.61	0.25	0.02
SOA	0.00	0.48	0.49	0.03
MOA	0.00	0.01	0.39	0.60
HOA	0.00	0.00	0.32	0.68

The average lengths of the needle-like precipitates for the SOA, MOA, and HOA treatments are measured to be approximately 35 nm, 128 nm, and 135 nm, respectively. The over-aging treatment promotes the growth and coarsening of needle-like precipitates. The increases in the average size of the over-aged alloys indirectly suggest that the matrix precipitates are dissolving during over-aging. Consequently, compared to those of the T6-treated alloys, the number of densities and volume fractions of over-aged alloys would decrease, as reported in the literature [4,33].

Among the precipitates distributed in the matrix, the  $\beta''$  phase exhibits a higher strengthening effect than the GP zones, and the  $\beta'$ ,  $B'$ , and disordered phases.

### 3.3. TEM and HRTEM Overviews of Precipitates at/near the Grain Boundaries

The effects of heat treatment on the grain boundary precipitates (GBPs) of the aged samples can be analyzed based on Figures 12 and 13. Figure 12 illustrates the bright-field TEM images near the grain boundaries in the T6, RRA, and T78 samples. To accurately characterize the difference in the precipitate-free zone (PFZ) widths with aging temper, one grain near the grain boundaries is tilted to be parallel to the  $\langle 001 \rangle_{\text{Al}}$  axis. The PFZ widths of the T6, RRA, and T78 samples are measured to be approximately 10 nm, 155 nm, and 182 nm, respectively.

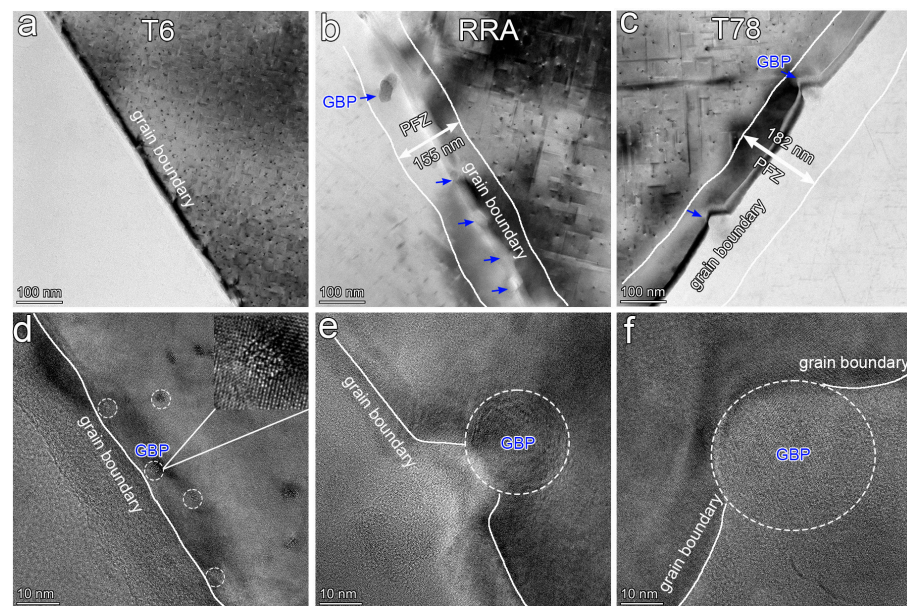


**Figure 12.** Bright-field TEM images and HRTEM images of the typical grain boundary structures in a 6016 alloy subjected to (a,d) T6, (b,e) RRA, and (c,f) T78 tempers.

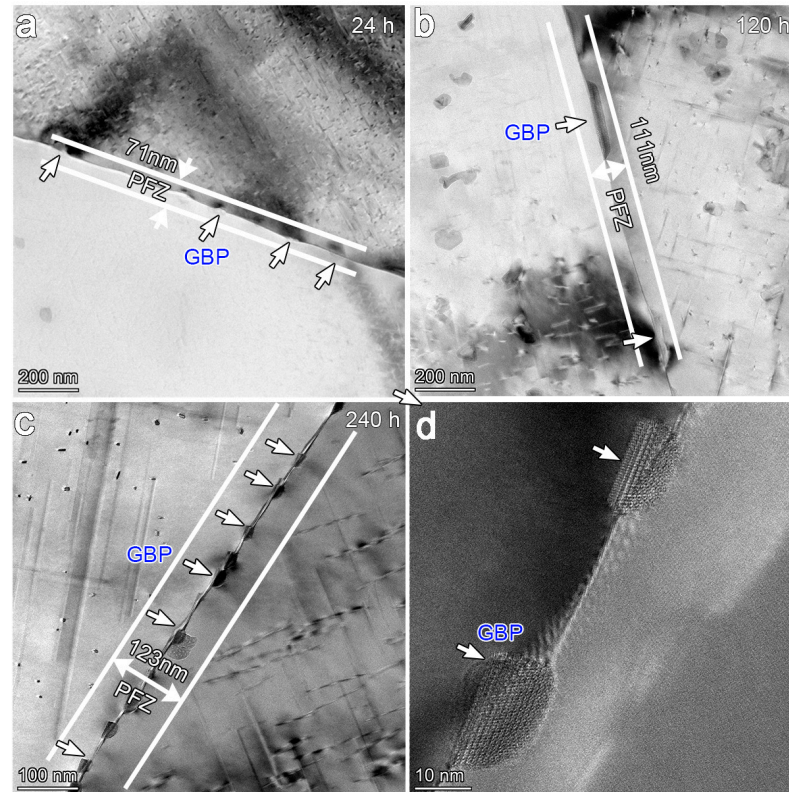
It is observed that the T6-6016 alloy exhibits finer GBPs adjacent to the grain boundaries and narrower PFZs, as shown in Figure 12a,d. Conversely, both the GBPs and their intervals become coarser in both the RRA (Figure 12b,e) and T78 (Figure 12c,f) treatments. Notably, the PFZ width of the T78 temper is larger than that of the RRA temper. The increase in the widths of the PFZs of the RRA and T78 treated alloys indirectly indicates that the matrix precipitates near the PFZs dissolve during the RRA and T78 treatments.

Figure 13 displays the bright-field TEM images near the grain boundaries in the slightly, moderately, and severely over-aged samples. The widths of the PFZs in the SOA, MOA, and HOA samples are measured to be approximately 71 nm, 111 nm, and 123 nm, respectively.

It can be summarized that the GBPs grow continuously as the aging times increase up to 5 days. Consequently, the number density of the GBPs decreases, and the distance between the GBPs increases. However, the distance between the GBPs notably decreases when the aging time increases to 10 days (with the HOA temper). This decreased distance between the GBPs is likely due to the dissolution of the existing precipitates in the grain interiors and the re-precipitation of the GBPs when the samples undergo long-term aging treatment, such as the 10-day duration in this study.

From a thermodynamic standpoint, the re-precipitation along the grain boundary is energetically more favorable than re-precipitation in the grain interior. When some precipitates dissolve after long-term aging, the solute atoms in the Al matrix become scarce compared to the supersaturation after quenching. Consequently, the driving force for re-

precipitation in the grain interior is insufficient. Conversely, the grain boundary provides nucleation sites for these free solute atoms. In this study, the re-precipitation of GBPs competes with the coarsening of precipitates in the grain interior, at the expense of the dissolution of some precipitates.



**Figure 13.** Images of the typical grain boundary regions in a 6016 alloy subjected to over-aged treatment at 180 °C. (a) SOA; (b) MOA; and (c,d) HOA.

Energy dispersive spectroscopy (EDS) mappings of grain boundaries and matrix precipitates in the HOA sample are depicted in Figures 14 and 15, respectively. The EDS mappings reveal that the GBPs contain Al, Mg, Si, and/or Cu elements, while the matrix precipitates mainly consist of Al, Mg, and Si elements. Consequently, during the HOA process, the Cu elements could segregate at the grain boundaries and form the GBPs.

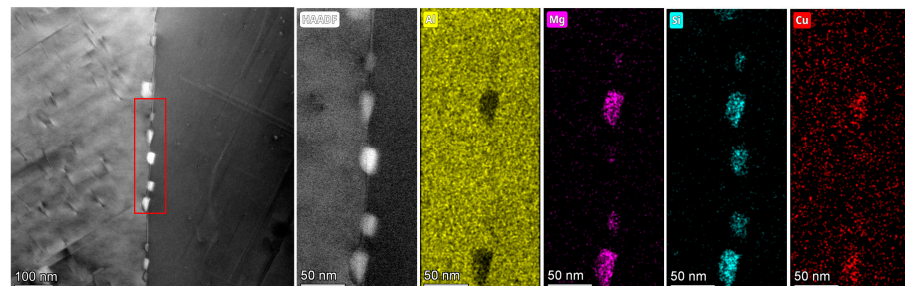


**Figure 14.** HAADF images and corresponding Al, Mg, Si, and Cu mappings of the typical grain boundary regions in a 6016 alloy subjected to HOA treatment.

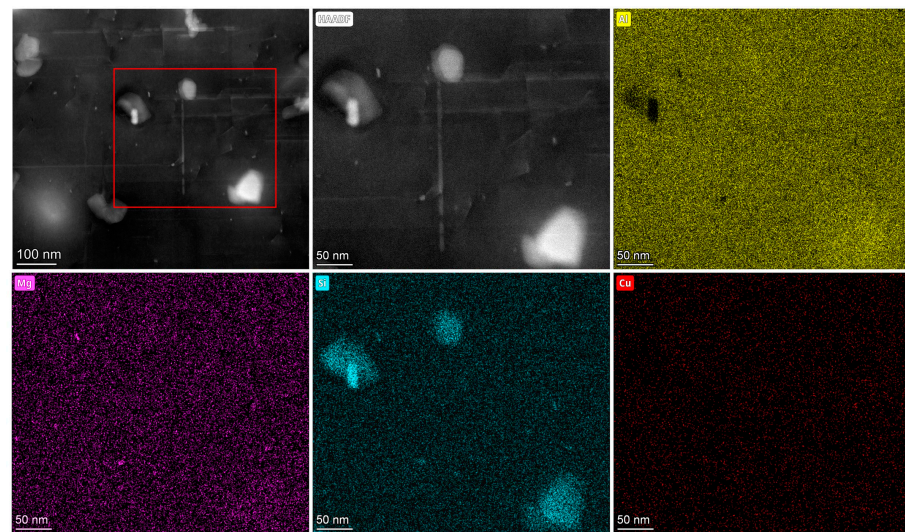


**Figure 15.** HAADF images and corresponding Al, Mg, Si, and Cu mappings of the typical matrix in a 6016 alloy subjected to HOA treatment.

These EDS mappings suggest that Cu atoms play a crucial role in the re-precipitation process during long-term aging treatments.

It is well acknowledged that the occurrence of GBPs and a PFZ is attributed to the migration of solute atoms towards grain boundaries, which are highly susceptible to the heat treatment process [29,35,43–45]. During a high temperature aging treatment (195 °C), previously formed precipitates dissolve first, causing solute atoms to migrate toward the grain boundaries. Subsequent aging treatments facilitate the easy formation of precipitates adjacent to or at grain boundaries. This migration of solute atoms to the grain boundaries and the subsequent formation of GBPs results in a solute atom-depleted zone adjacent to the grain boundaries [33,46]. The formation of this solute atom-depleted zone can be utilized to explain the formation of the PFZ observed in the samples.

Matrix and grain boundary microstructures of the T6, RRA, T78, and over-aging treated samples are shown in Table 4.

**Table 4.** Matrix and grain boundary microstructures of the T6, RRA, T78, and over-aging treated samples.

Aging Condition	Types of Matrix Precipitates	Width of PFZ (nm)	Average Length of Needle-Like Phases (nm)
T6	GP zones + $\beta''$ phase	<10	16
180 °C × 10 h + 195 °C × 0.5 h	GP zones + $\beta''$ phase		24
RRA	$\beta''$ + lath-like $\beta'$ + disordered phases	155	48
T78	$\beta''$ + B' + disordered phases	182	38
SOA	$\beta''$ + B' + disordered phases	71	35
MOA	B' + lath-like $\beta'$ + $\beta''$ /disordered composite phases	111	128
HOA	B' + B'/disordered composite + disordered phases	123	135

### 3.4. The Relationship between Microstructures and Hardness

The T6-treated sample exhibits the highest hardness due to the dense  $\beta''$  phases [10]. In contrast, the SOA sample (Figure 2) experiences a slight decrease in hardness as the precipitates coarsen, reducing the volume density. Notably, the MOA condition sees a significant decrease in hardness (Figure 2) due to an obvious coarsening of the precipitates (Table 4) and a reduced volume density. Furthermore, changing the precipitate types also hinders the dislocation movement, contributing to a reduced hardness (Table 4).

In the case of the SOA treatment, the precipitates undergo significant coarsening, shifting from a cutting to a bypassing mechanism [42]. Consequently, the volume fraction decreases, hindering the dislocation movement further, and leading to a reduced hardness. Additionally, the wider PFZs during over-aging treatments also contribute to a decreased hardness.

The RRA and T78 treatments (Figure 2) have a slightly lower hardness than the T6 but are notably higher than the MOA and HOA treatments. However, they feature wider PFZs (Table 4) and slightly larger precipitate sizes than the T6 and SOA samples. Wide PFZs (>71 nm) significantly impact the yield strength, contributing over half of the strengthening effect compared to intragranular precipitates [4]. Therefore, the wider PFZs and coarser precipitates lead to a decreased hardness in the RRA and T78 treatments compared to the T6 and SOA samples.

Statistical results show that the RRA and T78-treated alloys have smaller nano-sized (<10 nm) precipitates (Table 3) than the T6 and SOA-treated ones. During high temperature aging, the precipitate types mainly comprise GP zones and needle-like  $\beta''$  phases. While  $\beta''$  phases grow during aging treatments, the number of small-sized precipitates remains similar to the T6 treatment, but the medium-sized phases decrease and the large-sized precipitates increase.

According to the above statistical results, we deduce that retrogression in Al-Mg-Si-Cu alloys involves partial GP zone dissolution and  $\beta''$  phase re-precipitation during re-aging treatment at high temperatures in the RRA. Small nano-sized precipitates nucleate during high temperature aging and grow during further aging, compensating for hardness loss due to wider PFZs and decreased precipitate strengthening (Table 4).

The T78 and RRA-treated samples have a slightly lower hardness than the T6 due to finer precipitates compensating for the width increase in the PFZ and the precipitate strengthening decrease. In contrast, moderate and severe over-aging treatments have narrower PFZs but significantly coarsened intragranular precipitates, leading to a decreased hardness compared to the T78 and RRA.

Despite slight over-aging, the T78 exhibits a slightly higher hardness than the RRA due to finer intragranular precipitates compensating for coarser GBPs and a wider PFZ (Table 4). Precipitation strengthening in the matrix has a larger impact on mechanical properties, resulting in a higher hardness for the T78.

#### 4. Conclusions

This study investigated the relationship between the microstructures and mechanical properties of an Al-Mg-Si-Cu alloy subjected to various aging treatments: peak aging (T6), retrogression and re-aging (RRA), two-step aging (T78), slight over-aging (SOA), moderate over-aging (MOA), and heavy over-aging (HOA). The following conclusions were drawn:

- (1) The T6 treatment exhibited the highest hardness due to the presence of a high density of fine needle-like  $\beta''$  strengthening effects.
- (2) The over-aging treatments resulted in the precipitation of lath-like  $\beta'$ ,  $\beta''$ /disordered, or  $B'$ /disordered composite phases. The MOA treatment caused the coarsening of the grain boundary precipitates (GBPs) and the widening of the PFZ, while the HOA treatment led to the re-precipitation of the Cu-containing GBPs and increased the GBP density. The RRA treatment precipitated  $\beta''$ , lath-like  $\beta'$ , and disordered phases, while the T78 treatment precipitated  $\beta''$ ,  $B'$ , and disordered phases. Both the T78 and RRA treatments led to the coarsening of the GBPs and the widening of the PFZs.
- (3) Decreased hardness during post-over-aging treatment was attributed to a combination of coarsening intragranular precipitates and/or wider precipitation-free zones (PFZs) and the change of precipitate types.
- (4) The T78 and RRA treatments achieved 95.5% and 94% of the hardness values of the T6 treatment (113 HV), respectively. The hardness of the T78 and RRA treatments was nearly equivalent to that of the SOA treatment.

- (5) The hardness of the RRA and T78 treated alloys depended on the presence of finer nano-sized (<10 nm) precipitates formed during the high temperature process. These finer nano-sized precipitates could compensate for the loss of hardness caused by the increase of the widths of the PFZs and the coarser matrix precipitates.

**Author Contributions:** Conceptualization, L.L.; methodology, L.L. and Y.H.; software, L.L.; validation, L.L., Y.H. and S.D.; formal analysis, L.L. and Y.H.; investigation, L.L., Y.H., Y.G. and X.H.; data curation, L.L., Y.H. and S.D.; writing—original draft preparation, L.L.; writing—review and editing, S.D., Y.G., X.H., Y.W., T.Y. and L.Z.; project administration, S.D., T.Y., C.L. and L.Z.; and funding acquisition, Y.W., S.D., T.Y., L.Z. and C.L. All authors have read and agreed to the published version of the manuscript.

**Funding:** This research was funded by the National Natural Science Foundation of China (52201074, 52171115), the Hunan Provincial Natural Science Foundation (Grants no. 2023JJ50111), the Hunan Provincial Science and Technology Talent Plan Project (Grants no. 2021RC1008), the Provincial Open Project of Applied Characteristic Discipline (KFA22012), the Hunan Provincial Department of Education Scientific Research Project (Grants nos. 21B0805, 21B0796 and 22C0626), the National College Students' Innovation and Entrepreneurship Training Program (Grants nos. 202211528007) and the Hunan Provincial College Students' Innovation and Entrepreneurship (S202311528101).

**Data Availability Statement:** The data presented in this study are available on request from the corresponding author. The data are not publicly available due to the data also forms part of an ongoing study.

**Conflicts of Interest:** The authors declare no conflicts of interest.

## References

- Ma, J.; Liu, X.; Yan, D.; Rong, L. A novel GP-Li precursor and the correlated precipitation behaviors in Al-Cu-Li alloys with different Cu/Li ratio. *Acta Mater.* **2023**, *243*, 118442. [[CrossRef](#)]
- Ma, Y.; Chen, H.; Zhang, M.-X.; Addad, A.; Kong, Y.; Lezaack, M.B.; Gan, W.; Chen, Z.; Ji, G. Break through the strength-ductility trade-off dilemma in aluminum matrix composites via precipitation-assisted interface tailoring. *Acta Mater.* **2023**, *242*, 118470. [[CrossRef](#)]
- Singh, P.; Ramacharyulu, D.A.; Kumar, N.; Saxena, K.K.; Eldin, S.M. Change in the structure and mechanical properties of Al-Mg-Si alloys caused by the addition of other elements: A comprehensive review. *J. Mater. Res. Technol.* **2023**, *27*, 1764–1796. [[CrossRef](#)]
- Yang, M.; Ruan, Z.; Lin, H.; Li, K.; Yang, M.; Wang, Z.; Lan, X.; Xie, Y.; Xiao, Y.; Yan, Q.; et al. Quantified effect of quench rate on the microstructures and mechanical properties of an Al-Mg-Si alloy. *J. Mater. Res. Technol.* **2023**, *24*, 6753–6761. [[CrossRef](#)]
- Abúndez, A.; Pereyra, I.; Campillo, B.; Serna, S.; Alcludia, E.; Molina, A.; Blanco, A.; Mayén, J. Improvement of ultimate tensile strength by artificial ageing and retrogression treatment of aluminium alloy 6061. *Mater. Sci. Eng. A* **2016**, *668*, 201–207. [[CrossRef](#)]
- Chen, X.P.; Mei, L.; Chen, D.; Bao, Z.L.; Liu, Q. The effect of initial aging treatment on the microstructure and mechanical properties of cryorolled 6016 Al alloy. *Mater. Sci. Eng. A* **2016**, *667*, 311–316. [[CrossRef](#)]
- Engler, O.; Marioara, C.D.; Aruga, Y.; Kozuka, M.; Myhr, O.R. Effect of natural ageing or pre-ageing on the evolution of precipitate structure and strength during age hardening of Al-Mg-Si alloy AA 6016. *Mater. Sci. Eng. A* **2019**, *759*, 520–529. [[CrossRef](#)]
- Ninive, P.H.; Strandlie, A.; Gulbrandsen-Dahl, S.; Lefebvre, W.; Marioara, C.D.; Andersen, S.J.; Friis, J.; Holmestad, R.; Løvvik, O.M. Detailed atomistic insight into the  $\beta''$  phase in Al-Mg-Si alloys. *Acta Mater.* **2014**, *69*, 126–134. [[CrossRef](#)]
- Marioara, C.D.; Andersen, S.J.; Jansen, J.; Zandbergen, H.W. The influence of temperature and storage time at RT on nucleation of the  $\beta''$  phase in a 6082 Al-Mg-Si alloy. *Acta Mater.* **2003**, *51*, 789–796. [[CrossRef](#)]
- Chen, J.H.; Costan, E.; Huis, M.A.V.; Xu, Q.; Zandbergen, H.W. Atomic Pillar-Based Nanoprecipitates Strengthen AlMgSi Alloys. *Science* **2006**, *312*, 416–419. [[CrossRef](#)]
- Marioara, C.D.; Andersen, S.J.; Stene, T.N.; Hasting, H.; Walmsley, J.; van Helvoort, A.T.J.; Holmestad, R. The effect of Cu on precipitation in Al-Mg-Si alloys. *Phil. Mag.* **2007**, *87*, 3385–3413. [[CrossRef](#)]
- Guo, M.; Sun, M.; Huang, J.; Pang, S. A Comparative Study on the Microstructures and Mechanical Properties of Al-10Si-0.5Mg Alloys Prepared under Different Conditions. *Metals* **2022**, *12*, 142. [[CrossRef](#)]
- Zhou, P.; Wang, D.; Nagaumi, H.; Wang, R.; Zhang, X.; Li, X.; Zhang, H.; Zhang, B. Microstructural Evolution and Mechanical Properties of Al-Si-Mg-Cu Cast Alloys with Different Cu Contents. *Metals* **2023**, *13*, 98. [[CrossRef](#)]
- Vissers, R.; van Huis, M.A.; Jansen, J.; Zandbergen, H.W.; Marioara, C.D.; Andersen, S.J. The crystal structure of the  $\beta'$  phase in Al-Mg-Si alloys. *Acta Mater.* **2007**, *55*, 3815–3823. [[CrossRef](#)]
- Chen, K.; Liu, C.; Yang, J.; Ma, P.; Zhan, L.; Huang, M.; Li, J. Stabilizing Al-Mg-Si-Cu alloy by precipitation nano-phase control. *Mater. Sci. Eng. A* **2020**, *769*, 110883. [[CrossRef](#)]

16. Liu, Y.; Lai, Y.X.; Chen, Z.Q.; Chen, S.L.; Gao, P.; Chen, J.H. Formation of  $\beta''$ -related composite precipitates in relation to enhanced thermal stability of Sc-alloyed Al-Mg-Si alloys. *J. Alloys Compd.* **2021**, *885*, 160942. [[CrossRef](#)]
17. Lai, Y.X.; Fan, W.; Yin, M.J.; Wu, C.L.; Chen, J.H. Structures and formation mechanisms of dislocation-induced precipitates in relation to the age-hardening responses of Al-Mg-Si alloys. *J. Mater. Sci. Technol.* **2020**, *41*, 127–138. [[CrossRef](#)]
18. Hasting, H.S.; Frøseth, A.G.; Andersen, S.J.; Vissers, R.; Walmsley, J.C.; Marioara, C.D.; Danoix, F.; Lefebvre, W.; Holmestad, R. Composition of  $\beta''$  precipitates in Al-Mg-Si alloys by atom probe tomography and first principles calculations. *J. Appl. Phys.* **2009**, *106*, 12. [[CrossRef](#)]
19. Torsæter, M.; Hasting, H.S.; Lefebvre, W.; Marioara, C.D.; Walmsley, J.C.; Andersen, S.J.; Holmestad, R. The influence of composition and natural aging on clustering during preaging in Al-Mg-Si alloys. *J. Appl. Phys.* **2010**, *108*, 7. [[CrossRef](#)]
20. Andersen, S.J.; Marioara, C.D.; Frøseth, A.; Vissers, R.; Zandbergen, H.W. Crystal structure of the orthorhombic U2-Al4Mg4Si4 precipitate in the Al-Mg-Si alloy system and its relation to the  $\beta'$  and  $\beta''$  phases. *Mater. Sci. Eng. A* **2005**, *390*, 127–138. [[CrossRef](#)]
21. Saito, T.; Marioara, C.D.; Andersen, S.J.; Lefebvre, W.; Holmestad, R. Aberration-corrected HAADF-STEM investigations of precipitate structures in Al-Mg-Si alloys with low Cu additions. *Philos. Mag.* **2013**, *94*, 520–531. [[CrossRef](#)]
22. Urban, K.W. Studying atomic structures by aberration-corrected transmission electron microscopy. *Science* **2008**, *321*, 506–510. [[CrossRef](#)] [[PubMed](#)]
23. Chen, H.; Lu, J.; Kong, Y.; Li, K.; Yang, T.; Meingast, A.; Yang, M.; Lu, Q.; Du, Y. Atomic scale investigation of the crystal structure and interfaces of the  $B'$  precipitate in Al-Mg-Si alloys. *Acta Mater.* **2020**, *185*, 193–203. [[CrossRef](#)]
24. Weng, Y.; Jia, Z.; Ding, L.; Du, K.; Duan, H.; Liu, Q.; Wu, X. Special segregation of Cu on the habit plane of lath-like  $\beta'$  and QP2 precipitates in Al-Mg-Si-Cu alloys. *Scr. Mater.* **2018**, *151*, 33–37. [[CrossRef](#)]
25. Li, K.; Béché, A.; Song, M.; Sha, G.; Lu, X.; Zhang, K.; Du, Y.; Ringer, S.P.; Schryvers, D. Atomistic structure of Cu-containing  $\beta''$  precipitates in an Al-Mg-Si-Cu alloy. *Scr. Mater.* **2014**, *75*, 86–89. [[CrossRef](#)]
26. Saito, T.; Muraishi, S.; Marioara, C.D.; Andersen, S.J.; Røyset, J.; Holmestad, R. The effect of low Cu additions and pre-deformation on the precipitation in a 6060 Al-Mg-Si alloy. *Metall. Mater. Trans. A* **2013**, *44*, 4124–4135. [[CrossRef](#)]
27. Torsæter, M.; Ehlers, F.J.H.; Marioara, C.D.; Andersen, S.J.; Holmestad, R. Applying precipitate-host lattice coherency for compositional determination of precipitates in Al-Mg-Si-Cu alloys. *Philos. Mag.* **2012**, *92*, 3833–3856. [[CrossRef](#)]
28. Sunde, J.K.; Marioara, C.D.; Holmestad, R. The effect of low Cu additions on precipitate crystal structures in overaged Al-Mg-Si(-Cu) alloys. *Mater. Charact.* **2020**, *160*, 110087. [[CrossRef](#)]
29. Schnatterer, C.; Zander, D. Influence of the grain boundary chemistry on the intergranular corrosion mechanisms of a high-strength Al-Mg-Si alloy. *Surf. Interface Anal.* **2016**, *48*, 750–754. [[CrossRef](#)]
30. Pan, D.; Wang, Z.; Li, H.; Zheng, Z.Q. Effects of two-step ageing treatment on tensile properties and intergranular corrosion of 6061 aluminum alloy. *Chin. J. Nonferrous Met.* **2010**, *20*, 435–441.
31. Wang, Z.; Zhu, F.; Zheng, K.; Jia, J.; Wei, Y.; Li, H.; Huang, L.; Zheng, Z. Effect of the thickness reduction on intergranular corrosion in an under-aged Al-Mg-Si-Cu alloy during cold-rolling. *Corros. Sci.* **2018**, *142*, 201–212. [[CrossRef](#)]
32. Li, H.; Qingzhong, M.; Wang, Z.; Miao, F.; Fang, B.; Song, R.; Zheng, Z. Simultaneously enhancing the tensile properties and intergranular corrosion resistance of Al-Mg-Si-Cu alloys by a thermo-mechanical treatment. *Mater. Sci. Eng. A* **2014**, *617*, 165–174. [[CrossRef](#)]
33. Li, H.; Zhao, P.; Wang, Z.; Mao, Q.; Fang, B.; Song, R.; Zheng, Z. The intergranular corrosion susceptibility of a heavily overaged Al-Mg-Si-Cu alloy. *Corros. Sci.* **2016**, *107*, 113–122. [[CrossRef](#)]
34. Li, X.; Chen, J.; Liu, C.; Feng, J.; Wang, S. Effects of T6 and T78 tempers on the microstructures and properties of Al-Mg-Si-Cu alloys. *Acta Metall. Sin.* **2013**, *49*, 243–250. [[CrossRef](#)]
35. Liu, L.; Lai, Y.; Liu, C.; Chen, J. Optimized combinatorial properties of an AlMgSi(Cu) alloy achieved by a mechanical-thermal combinatorial process. *Acta Metall. Sin.* **2018**, *33*, 751–758. [[CrossRef](#)]
36. Guillaumin, V.; Mankowski, G. Influence of Overaging Treatment on Localized Corrosion of Al 6056. *Corrosion* **2000**, *56*, 12–23. [[CrossRef](#)]
37. Li, G.; Zhang, X.; Li, P.; You, J. Effects of retrogression heating rate on microstructures and mechanical properties of aluminum alloy 7050. *Trans. Nonferrous Met. Soc. China* **2010**, *20*, 935–941. [[CrossRef](#)]
38. Li, J.F.; Birbilis, N.; Li, C.X.; Jia, Z.Q.; Cai, B.; Zheng, Z.Q. Influence of retrogression temperature and time on the mechanical properties and exfoliation corrosion behavior of aluminium alloy AA7150. *Mater. Charact.* **2009**, *60*, 1334–1341. [[CrossRef](#)]
39. Oliveira, A.F.; de Barros, M.C.; Cardoso, K.R.; Travessa, D.N. The effect of RRA on the strength and SCC resistance on AA7050 and AA7150 aluminium alloys. *Mater. Sci. Eng. A* **2004**, *379*, 321–326. [[CrossRef](#)]
40. Peng, G.; Chen, K.; Chen, S.; Fang, H. Influence of repetitious-RRA treatment on the strength and SCC resistance of Al-Zn-Mg-Cu alloy. *Mater. Sci. Eng. A* **2011**, *528*, 4014–4018. [[CrossRef](#)]
41. Xiao, Y.P.; Pan, Q.L.; Li, W.B.; Liu, X.Y.; He, Y.B. Influence of retrogression and re-aging treatment on corrosion behaviour of an Al-Zn-Mg-Cu alloy. *Mater. Des.* **2011**, *32*, 2149–2156. [[CrossRef](#)]
42. Tao, G.H.; Liu, C.H.; Chen, J.H.; Lai, Y.X.; Ma, P.P.; Liu, L.M. The influence of Mg/Si ratio on the negative natural aging effect in Al-Mg-Si-Cu alloys. *Mater. Sci. Eng. A* **2015**, *642*, 241–248. [[CrossRef](#)]
43. Ma, P.; Liu, C.; Chen, Q.; Wang, Q.; Zhan, L.; Li, J. Natural-ageing-enhanced precipitation near grain boundaries in high-strength aluminum alloy. *J. Mater. Sci. Technol.* **2020**, *46*, 107–113. [[CrossRef](#)]

44. Zou, Y.; Liu, Q.; Jia, Z.; Xing, Y.; Ding, L.; Wang, X. The intergranular corrosion behavior of 6000-series alloys with different Mg/Si and Cu content. *Appl. Surf. Sci.* **2017**, *405*, 489–496. [[CrossRef](#)]
45. Kairy, S.K.; Alam, T.; Rometsch, P.A.; Davies, C.H.J.; Banerjee, R.; Birbilis, N. Understanding the Origins of Intergranular Corrosion in Copper-Containing Al-Mg-Si Alloys. *Metall. Mater. Trans. A* **2016**, *47*, 985–989. [[CrossRef](#)]
46. Svenningsen, G.; Larsen, M.H.; Walmsley, J.C.; Nordlien, J.H.; Nisancioglu, K. Effect of artificial aging on intergranular corrosion of extruded AlMgSi alloy with small Cu content. *Corros. Sci.* **2006**, *48*, 1528–1543. [[CrossRef](#)]

**Disclaimer/Publisher’s Note:** The statements, opinions and data contained in all publications are solely those of the individual author(s) and contributor(s) and not of MDPI and/or the editor(s). MDPI and/or the editor(s) disclaim responsibility for any injury to people or property resulting from any ideas, methods, instructions or products referred to in the content.